Available online at www.sciencedirect.com
ScienceDirect
Nuclear Instruments and Methods in Physics Research A 586 (2008) 133–142
NUCLEAR INSTRUMENTS & METHODS IN PHYSICS RESEARCH Section A
www.elsevier.com/locate/nima

A bi-periodic X-Band cavity for SPARC

B. Spataro[a,*], D. Alesini[a], A. Bacci[c], L. Ficcadenti[a,b], A. Mostacci[a,b], L. Palumbo[a,b], R. Parodi[d]

[a]*INFN, Laboratori Nazionali di Frascati, Frascati, Italy*
[b]*Università di Roma "La Sapienza", Rome, Italy*
[c]*INFN, Milano-INFN, Milan, Italy*
[d]*INFN, Genova-INFN, Genova, Italy*

Received 26 July 2007; received in revised form 8 October 2007; accepted 23 October 2007
Available online 4 November 2007

Abstract

In order to produce a high brightness electron beam for the Frascati Linac coherent light source (SPARC) the use of an accelerating section with frequency equal to the fourth harmonic of the main S-Band Linac frequency is needed. This paper discusses the design and the realization of a compact X-Band linear accelerating section for obtaining 5 MV average accelerating gradient, working at a frequency of 11.424 GHz and operating on the $\pi/2$ standing wave mode. Numerical predictions compared with measurements made on a copper prototype at room temperature are reported.

PACS: 41.75.−i; 41.60.Cr

Keywords: High-brightness beams; Soft X-ray FEL; RF cavities for particle accelerators

1. Introduction

In order to enhance the bunch compression performances in SPARC [1], a linear longitudinal phase space for producing a high brightness electron beam is required. To compensate the non-linearity distortions due to the RF field curvature of the 2.856 GHz accelerating cavities during the acceleration and compression, the use of an additional X-Band accelerating structure operating at 11.424 GHz is needed to correct locally the RF curvature and to avoid the increase of the longitudinal emittance which limit the current growing [2]. The design of linear accelerating structures at high frequency is defined in a broader perspective by resulting from a compromise among several factors as beam dynamics, RF power sources, fabrication constraints, sensitivity to machining errors and so on.

The SPARC phase II schematic layout is reported in Fig. 1. The scheme is mainly constituted by

- 1.6 cell RF gun of the BNL/UCLA/SLAC type [3] which works in the S-Band at a frequency $f_s = 2.856$ GHz and generates bunches with a 5 MeV kinetic energy, 1 nC charge and 10 ps bunch length;
- an X-Band accelerating structure operating at a frequency $f = 11.424$ GHz [4];
- one S-Band velocity buncher (SLAC type section) [4];
- two S-Band accelerating traveling constant gradient sections (SLAC type sections).

The fourth harmonic frequency of the main Linac one has been chosen for space availability reasons and because the technologies in the X-Band power sources and modulators have been developed at KEK and SLAC for future linear collider projects [5–10].

RF stability during the operation and tuning tolerances are crucial points for the RF section design in this high frequency range. The complexity of machining, tight

*Corresponding author. Tel.: +39 0694032253; fax: +39 0694032256.
E-mail address: bruno.spataro@lnf.infn.it (B. Spataro).

0168-9002/$ - see front matter © 2007 Published by Elsevier B.V.
doi:10.1016/j.nima.2007.10.040

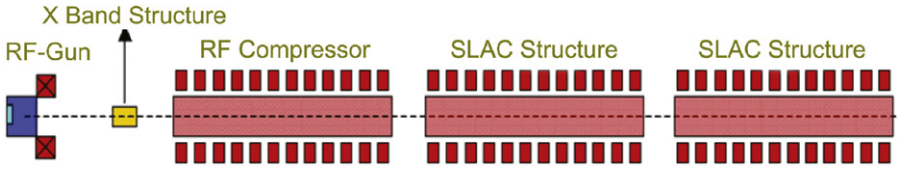

Fig. 1. Lay-out of the first part of the SPARC project.

Table 1
Requirements of the accelerating structure and beam parameters

Accelerating voltage	V	5 MV
Length	ℓ	12 cm
Beam aperture diameter	ϕ	8 mm
Operating frequency	f	11.424 GHz
Pulse charge	Q	1 nC
Full pulse length	τ	10 ps
Pulse repetition rate frequency	f_{REP}	50 Hz

mechanical tolerances and alignment are therefore important aspects which have to be taken into account in the design activity. The bi-periodic $\pi/2$ mode is particularly attractive since it gives rise to a good field stability against unwanted perturbations, even though it is more expensive and difficult to make as it will described in the following section. The requirements of the accelerating structure and beam parameters are shown in Table 1.

A fourth harmonic frequency of the one used in the main accelerator implies small physical sizes of the section and thereby the dissipated power constitutes one of the main constraints. A reasonable upper limit on the average power dissipation has been estimated to be around at 4 kW/m. By assuming 3 MW input peak power with a duty cycle of 10^{-4}, to get roughly 5 MV average accelerating voltage (42 MV/m average accelerating gradient), about 69 MΩ/m with a 2.7 kWm dissipated power are needed. Operation with quality factor Q sufficiently high of the section is also required for preventing the excitation of its neighboring modes.

The beam dynamic is not affected by the long-range wake-fields because the scheme operates with a single bunch. As a consequence no dedicated dampers of the parasitic higher order modes of the X-Band accelerator will be adopted. For meeting the global requirements by keeping a flexibility margin, a standing wave structure working on the $\pi/2$ mode with simpler geometry (axial coupling cells) that is cheap, reliability of construction and with satisfactory mechanical tolerances has been investigated in detail. As it will be described in the next sections, the designed X-Band structure to obtain 42 MV/m accelerating gradient is a 17 cells bi-periodic $\pi/2$ mode section with axial coupling cells and fed by a central coupler.

2. Cavity design

A bi-periodic structure can be designed with a side-coupling cells [11] or axial coupling cells [12]. Since the

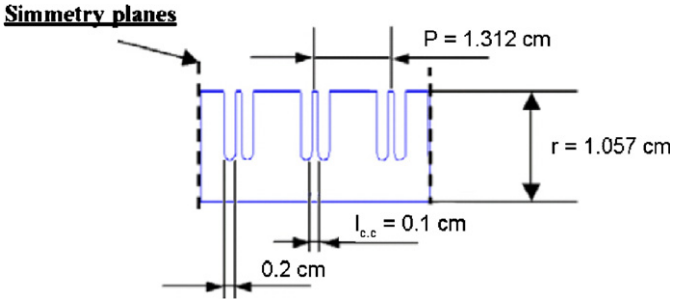

Fig. 2. Longitudinal section of the (opened stop-band) cavity.

side-coupled cavities increase the number matching and assembly steps, the present design is addressed to use a bi-periodic section with coupling cells mounted on the longitudinal axis—for a easier construction and economic reasons.

The reduced available space, the imposed irises beam aperture and the operating frequency, the power loss, dictated the physical dimensions of the uniform structure [13] showed in Fig. 2. The evaluations in frequency domain were performed by using OSCAR2D [14] and the SUPERFISH [15] computations codes.

2.1. Open and closed stop-band calculations

In order to reduce the computation effort and to determine with accuracy the results, the simulations were carried out on a half period of the cells with the proper symmetry planes and using smaller meshes. The double periodicity of the structure operating on $\pi/2$ mode introduces a stop band in the dispersion curve due to the two different electromagnetic fields distributions of the two $\pi/2$ modes resonances. In other words there are two resonant modes with the same cell-to-cell phase shift $\Phi = \pi/2$: one of them excites the long or accelerating cavity, while the other one excites the short or coupling cavity. The two $\pi/2$ modes electric field lines configurations obtained with the magnetic and electric mirror boundary conditions on the symmetry planes, are shown in Fig. 3. As a first result, the stop-band frequency range estimation is given by 1.67 GHz. Additional qualitative checks performed by using the well-known analytical lumped parameter model confirmed the numerical results relative to the two $\pi/2$ modes resonance [12]. In order to get the same frequencies resonances of the two $\pi/2$ modes to produce the closed stop band, the short cavity radius increase is needed. The corresponding cell sizes, field distributions of the accelerating and coupling cells, are depicted in Fig. 4.

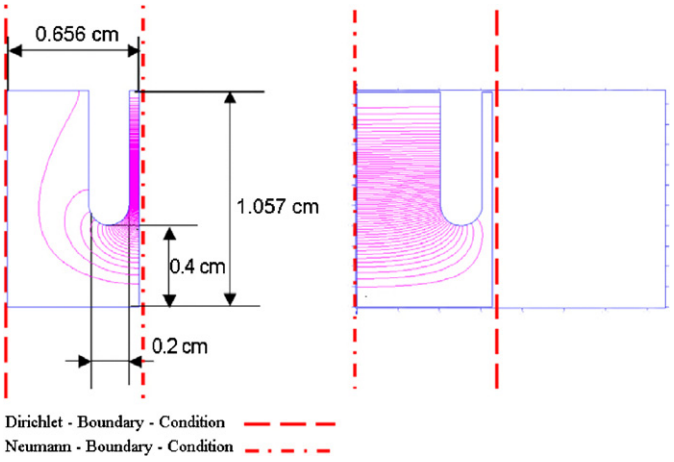

Fig. 3. Half cell simulated structure for the open stop-band estimation. The resonance frequency is 13.07086 GHz if the Neumann boundary condition is applied to the coupling cell (left picture). If the Neumann boundary condition is applied to the main cell, then the resonance frequency is 11.42357 GHz (right picture).

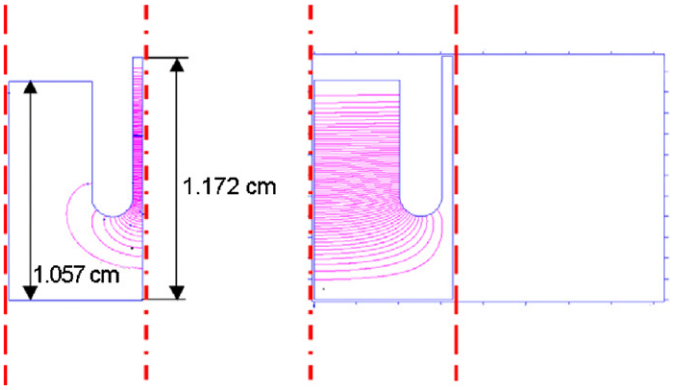

Fig. 4. Half cell simulated structure for the close stop-band estimation. The resonance frequency is 11.42424 GHz if the Neumann boundary condition is applied to the coupling cell (left picture). If the Neumann boundary condition is applied to the main cell, then the resonance frequency is 11.42433 GHz (right picture).

Moreover, the frequency global sensitivity due to the mechanical tolerances as function of the cavity radius has been evaluated to be around at $\Delta f = 1.8\,\mathrm{MHz}/\mu\mathrm{m}$.

2.2. Dispersion curve determination

The structure is constituted by nine accelerating cells and eight coupling cells. In Fig. 5 we represent the structure section sizes with the symmetry planes, that is electric (on the left side) and magnetic (on the right side) mirror; in Fig. 6 are reported the real section sizes with the coupling tubes. In the last picture the end cell has been tuned decreasing their radius, to compensate the perturbation introduced by beam tubes [16]. A check to verify the dispersion curves stability of the two structures is illustrated in Fig. 7. By comparing the two dispersion curves, their behavior substantially does not change and no

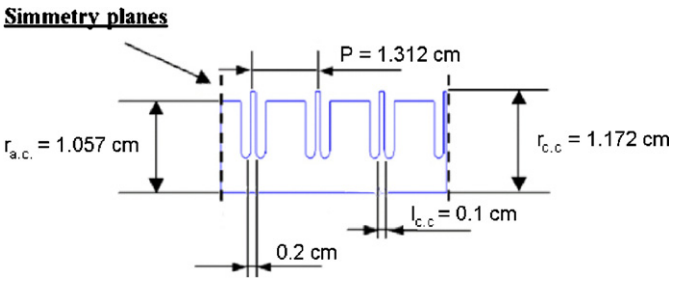

Fig. 5. Longitudinal section of the closed stop-band cavity with the symmetry planes.

significant frequencies deviation have been produced, as on the other hand it is expected to be. In particular, in the real structure the small frequencies shift are mainly due to the coupling tubes boundary conditions on which it is not possible to define a perfect electric or magnetic mirror. As an example, this fact is visible for the first 0-mode like. The frequencies separation between the operating $\pi/2$ mode frequency and the adjacent ones frequencies is about given by $\Delta f = 39\,\mathrm{MHz}$ and $\Delta f = 36\,\mathrm{MHz}$ against the operating mode bandwidth $\Delta f = 1.5\,\mathrm{MHz}$. In addition, from the spacing of the lower and upper cut-off frequencies, the coupling coefficient [13] is given by $\mathrm{K} = 3.63\%$. As a conclusion, in the real section the dispersion curve behavior and the working $\pi/2$ mode give a safety margin to assure a satisfactory operation stability.

2.3. Working mode

The average accelerating voltage for the design is imposed to be at 5 MeV and it has to be achieved with a good field flatness on the longitudinal axis. As it is above-mentioned, one of the basic requirements of the section is the power dissipation. In Fig. 8 is reported the electric field distribution profile on the longitudinal axis of the accelerating $\pi/2$ mode, assuming the multi-cell standing wave structure of Fig. 5 with beam tubes having a 8 mm diameter. By the inspection of the figure, the field flatness is clearly not achieved, calculating a 16% difference between the maximum and minimum peak. In order to get the field compensation on the axis the procedure reported by other authors is followed [16]. The end cells have been engineered lowering of 18 μm their radius for obtaining at $\pi/2$ mode a field flatness on axis as it is shown in Fig. 9. The real section is shown in Fig. 6. In Table 2 the relevant RF parameters are also reported. A $R_{sh} = 69\,\mathrm{M\Omega/m}$ shunt impedance for unit length, which measures the accelerating quality of the section, gives a satisfactory average power loss around 300 W by assuming an operation with a 10^{-4} duty cycle. We believe that the presence of non-resonant electron loading or dark current gives no specific trouble since the estimation of the average accelerating electric field is a 30% lower than one field limit threshold measured at SLAC [9]. In addition, the estimate of the energy spread due to beam loading was calculated

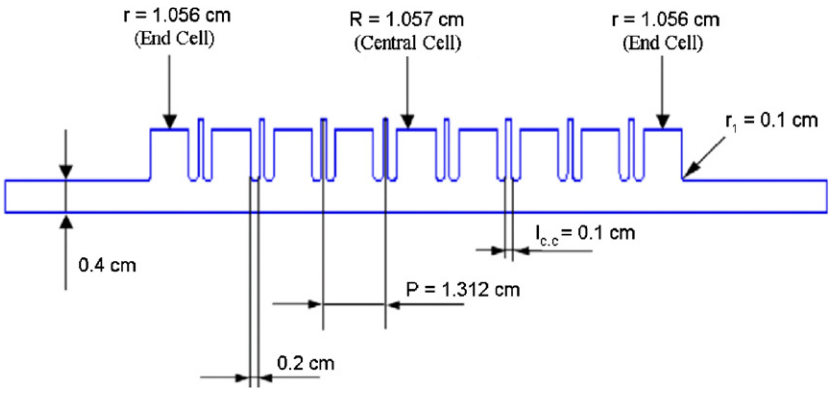

Fig. 6. Longitudinal real section of the cavity with coupling tubes.

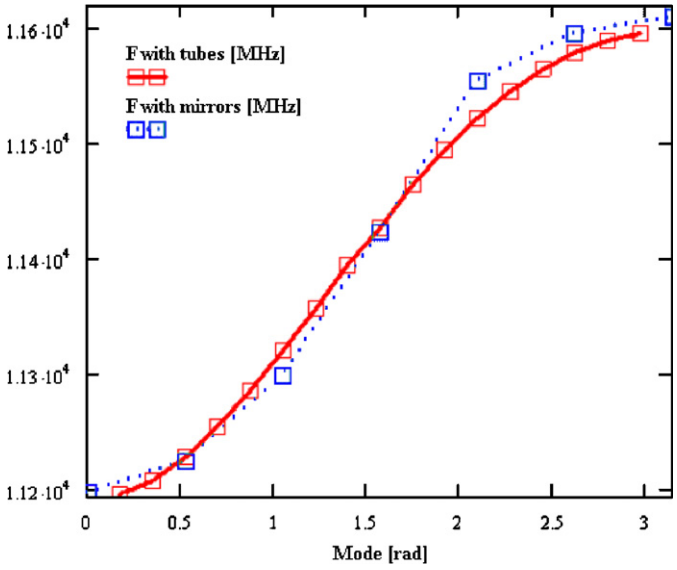

Fig. 7. Dispersion curves fit of the final shape.

with the analytical expression [13]. Assuming $R_{sh}/Q = 9693\,\Omega/m$, $N = 6.24 \times 10^9$ particles, $E_0 = 42\,MV/m$ and $f = 11.424\,GHz$, the energy spread is evaluated to be $\pm 0.825\%$. Additional simulations were carried out to estimate the shunt impedance R_{sh} as function of the coupling cell length L (by keeping closed the stop band and the structure periodicity). Getting an approximately linear behavior with slope $\Delta R_{sh}/\Delta L \approx -8\,(M\Omega/m)/mm$.

3. Electron discharge analysis

The propose $\pi/2$ X-Band accelerating structure developed for the SPARC Linac seems to be quite safe regarding both dark-current load and multipactoring (MP). Poor man computations, already proven true in accelerating structure, give some useful hints to evaluate the accelerating field level both for the onset of the electron loading and for the first order magnetic MP discharges at the accelerating cell equator. The structure geometry, with field lines superimposed, is shown in Fig. 10.

For pill box like cavities, the one point MP in the equator region is very well given by the expression [17]

$$B = \frac{2\pi f m}{n e} \tag{1}$$

where f is the field frequency, n is the MP threshold index, m the electron mass and e its charge. For the two point MP in the same region by

$$B = \frac{4\pi f m}{(2n-1)e} \tag{2}$$

leading to 28 mT per GHz and 56 mT per GHz for the first order MP level (i.e. $n = 1$).

In the SPARC X-Band Linac case, operating at 11.5 GHz gives discrete magnetic field values reported in Table 3: The surface magnetic field values are translated to accelerating electric field levels (including the Transit time factor) using the RF accelerating properties of the structure as computed by OSCAR2D or SUPERFISH. We report in Table 4 the first 5 MP barrier, remembering that usually, in a well conditioned RF accelerating structure only the first three barriers are likely to occur. The preliminary analysis performed in this way suggests us that the structure will run without serious MP problems up to $\simeq$ 15–20 MV/m of accelerating field. The assumption is verified using the TWTRAJ [18], the companion code of OSCAR2D [14], used to compute the RF properties of the accelerating structures. The analysis is performed in a statistical way on the basis of the resulting yield of the secondary re-emitted electrons surviving 100 impacts on the cavity walls for each field level between 1 and 40 MV/m (in step of 100 KV). At each field level the simulation starts computing the trajectories of the electrons till the cavity wall is hit. At this point a true secondary, a back scattered high energy electron or a scattered (elastic or inelastic) electron are re-emitted depending upon the impact energy, using a random generation accounting for the different end the cross-section for the competing processes at that energy. The re-emitted electrons start with energy and direction random generated following the energy end angle distribution of the reemission process. The electron trajectories are

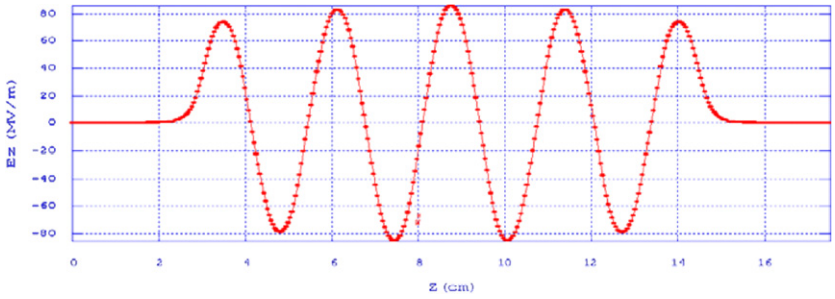

Fig. 8. Electric field profile of the accelerating mode without the electric field flatness.

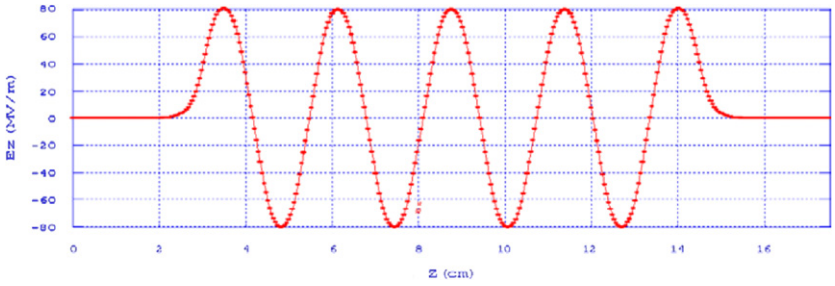

Fig. 9. Electric field profile of the accelerating mode with the electric field flatness.

Table 2
Relevant RF parameters

Frequency	f (MHz)	11 424
Length for calculation	ℓ (cm)	11.51
Cavities number	n_b	17
Structure periodicity	l_p (cm)	1.312
Beam hole radius	r (cm)	0.4
Iris thickness	t (cm)	0.2
Coupling coefficient	K (%)	3.63
Factor of merit	Q	7101
Form factor	R_{sh}/Q (Ω/m)	9693
Shunt impedance	R_{sh} (MΩ/m)	69
Peak power	P (MW)	2.95
Energy stored in cavity of length ℓ	W (J)	0.292
Duty cycle	D.C.	104
Repetition frequency	f (Hz)	50
Average accelerating field	E_{acc} (MV/m)	42
Peak axial electric field	E_{max} (MV/m)	55
Peak surface electric field	E_{sur} (MV/m)	102
Ratio of peak to average fields	E_{sur}/E_{acc}	2.43
Ratio of peak fields	B_{max}/E_{sur} (mT/MV/m)	1.9
Average beam power	P_{baver} (W)	0.242
Energy spread due to the beam loading	%	±0.828

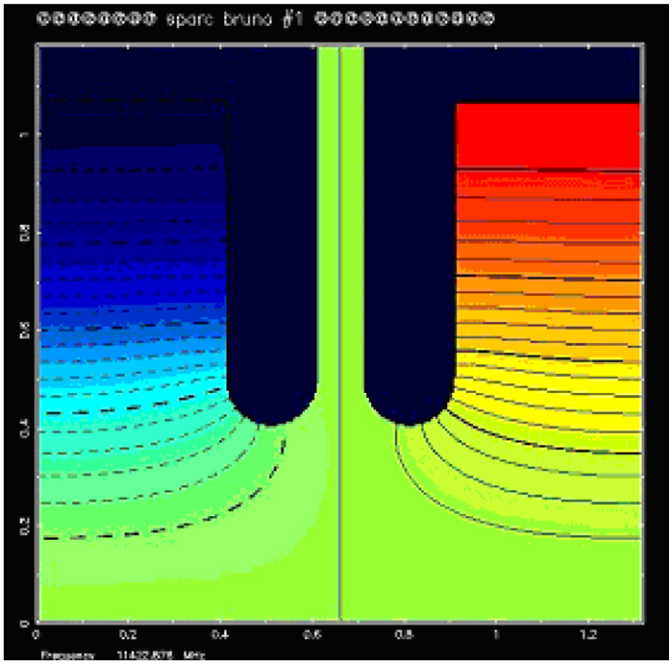

Fig. 10. $\pi/2$ accelerating structure unit cell.

followed for a number of impacts prefixed in the input data (usually 100) and the yield, impact energy and reemission energy at the impact recorded.

A specific electron trajectory is abandoned when:

- The time between two impacts is less than 10 RF degrees.
- The re-emitted electron yield is less than 0.1.
- The re-emitted electron energy is less than 0.1 eV.
- The electron leaves the accelerating cell (structure) via a beam hole.

Table 3
Expected values of the magnetic field for the first 5 MP barriers in accelerating structures at 11.5 GHz

	B field (mT) 2 points	B field (mT) 1 point
1	644	322
2	215	161
3	1129	107
4	92	81
5	72	65

Table 4
Expected values of the accelerating field for the first 5 MP barriers in accelerating structures at 11.5 GHz

	E field (MV/m) 2 points	E field (MV/m) 1 point
1	129	64
2	43	32
3	26	21
4	18	16
5	14	13

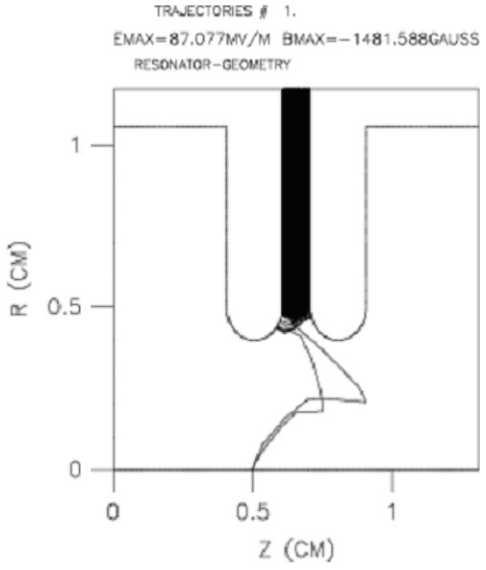

Fig. 11. Simulation of the electron trajectories in the "coupling cell" (800 electrons at an accelerating field level of $\simeq 30$ MV/m).

The yield and number of electrons surviving up to the prefixed impact number is used to computed the mean yield for the surviving electrons at a given field level. This mean yield is also used to compute the amount of energy drained by the electron trajectories and to evaluate the quality factor variation produced by the beam loading produced by the re-emitted electrons. In our case the result of the simulation clearly showed that in the given field range, no electrons are surviving up to 100 impacts, mainly due to a lack of energy gain along the trajectories between two impacts. In the main cells the electrons stay confined by the magnetic field in small paths close to the cell equator. The combined effect of small path and low radial E-field radial component, due to the sharp pill-box shape of the main cell, gives in maximum 10–20 impacts a secondary yield by far lower than 0.1 and the trajectory computation is stopped for all the 800 electrons considered. This behavior stays also increasing the number of starting electrons (and computation time) by a factor of 100.

Last we investigated the behavior of electrons starting close to the iris in the coupling cells between the main cells. For the $\pi/2$ mode still some possibility exists that trapped electron in the "empty" coupling cell can give rise to some discharge and instabilities at some field level.

The approach was similar to the used for the accelerating cells. The results are similar: emitted electrons die after some impact on the cavity walls drifting toward the cavity outer region, the combination of low electric an magnetic fields, together the field variation with radius and Z-coordinate, break for all the field level the resonant conditions producing the growth of the secondary electrons cloud and the successive field breakdown. A typical electron cloud for the "coupling" cell is shown in Fig. 11. The result of the simulations confirms the guess of no serious MP, nor electron discharges, in the accelerating structure for the operating range, and can either positively suggest that no electron activity will be encountered during operation.

4. 3D simulation results

HFSS [20] simulation codes have been used to design a proper feeding system for the cavity in the central cell in order not to excite the adjacent modes that have the nearest frequency to the $\pi/2$ mode and zero field in the central cell. Therefore with central coupler we have a much greater modes separation and the working mode is less perturbed by the closest ones. The coupling cell, coupler and window dimensions are sketched in Fig. 12. The dimension of the coupler window (w) and of the central cell radius (R_c) have been tuned in order to obtain simultaneously a coupling coefficient $\beta = 1$, a resonant frequency of the whole system equal to 11.424 GHz and to preserve a good field flatness. We have obtained the coupling coefficient $\beta = 0.97$ with a good field flatness, within few percent.

5. Prototype

Two full scale copper prototype has been constructed and it is shown in Fig. 13. The 17 cells structure has been designed for brazing, but the RF tests refer to a mechanically joined structure. The material used to build

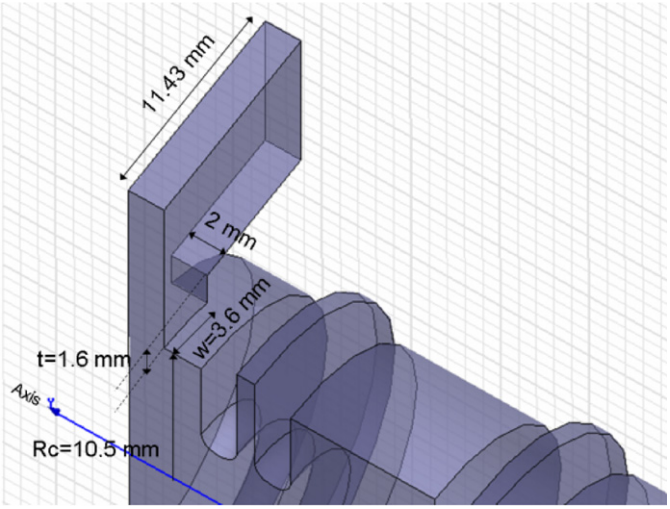

Fig. 12. Sketch of the coupling cell.

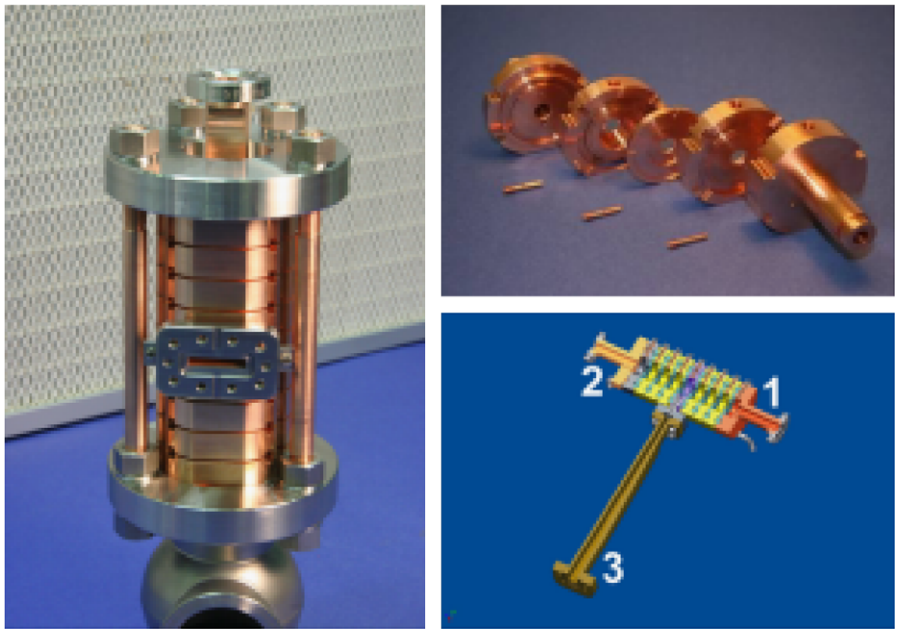

Fig. 13. Copper prototype of the structure.

this prototype is oxygen free copper. The structure has been realized by mechanical machining with a numerically controlled lathe and the obtained precision is below 0.01 mm, while the surface roughness is not worst than $0.4\,\mu R_a$. The assembling procedure foresees the joining of the 17 cells using two stainless disks used to press the structures by means of three 8 mm diameter copper rods. A torque of 11 N/m was applied to every rod, corresponding to a pressure of roughly $80\,\mathrm{N/mm^2}$. Each accelerating cell has a tuning screw (with 3 mm diameter and length of 5 mm, Fig. 13) to vary the cell volume and thus the resonant frequency and field distribution. The average frequency variation due to a 2 mm insertion of all the tuners is about 29 MHz. To feed the structure two lateral small antennas are also inserted (position 1, 2 of Fig. 13).

To check the mechanical realization procedure, two different types of structure have been realized and their electromagnetic properties measured. One can vary the frequency width of the stop band by increasing the radius of the coupling cells. When such a radius is identical to the one of the main cells, we expect to have an "opened" stop-band while increasing that radius we can arrive to a "closed" stop-band (i.e. no stop-band). A complete set of these two kinds of cells has been machined and they can be mounted in the prototype, eventually obtaining two different configurations: the opened stop-band structure and the closed stop-band structure.

6. Measurement results

Two type of different measurements have been carried out: transmission (or reflection) scattering coefficient measurements between the two antennas or between the antennas and the central coupler (port 3 in Fig. 13) and bead pull measurements.

The transmission coefficient between the two small lateral antennas and between the antennas and the central coupler has been measured both in the stop-band open and stop-band close structures. We can excite only nine over 17 possible modes by central coupler because we impose a non-zero field in the central cell. On the contrary with the two antennas we can excite all the possible modes.

The measured dispersion curve, compared with the one obtained from HFSS, GDFIDL and SUPERFISH, is reported in Fig. 14 showing a good agreement with the simulation results. The Q-factors of higher frequencies mode are not big enough to clearly distinguish the modes in the measurements.

The measurements of S-parameters allow the computation of mode frequencies and such measurements are reported in Figs. 15 and 16. The instrument screen-shot of the measurement of transmission coefficient between antennas placed in the side cells of the prototype for the opened stop-band structure is shown in Fig. 15. The frequency goes from 11.1 to 13.35 GHz and the difference between the two pass-bands is about 1.6 GHz, in agreement with the 1.67 GHz expected from numerical simulations (see Section 2.1).

On the contrary, the S_{12} measurement for the closed stop-band structure is reported in Fig. 16. The red line shows the transmission between one of the side cells and the central coupler and only the modes such that the field is non-zero in the central cell can be measured. On the contrary, by exciting the structure from the side cells, all the modes can be measured (as shown by the blue line). The coupler is designed to be in "critical coupling" (i.e. reflections are virtually null) while the probe antennas

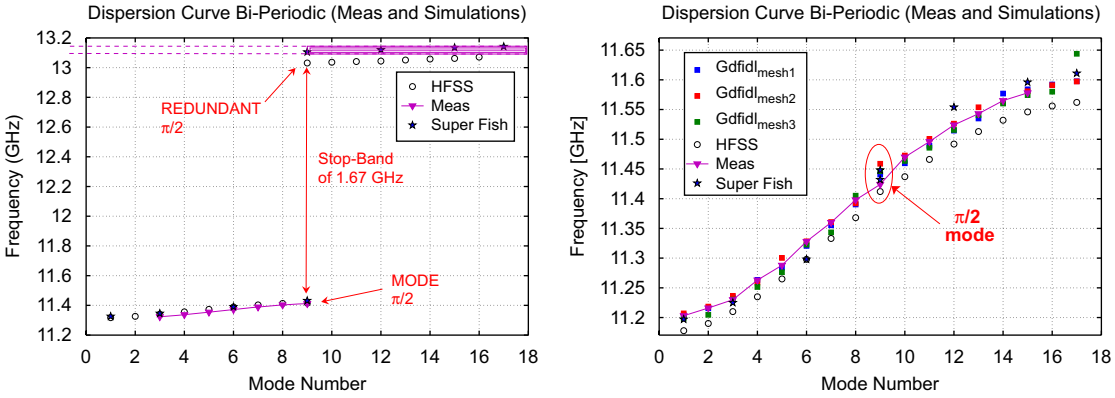

Fig. 14. Simulated and measured dispersion curve in the case *stop-band open* (left picture) and *stop-band close* (right picture).

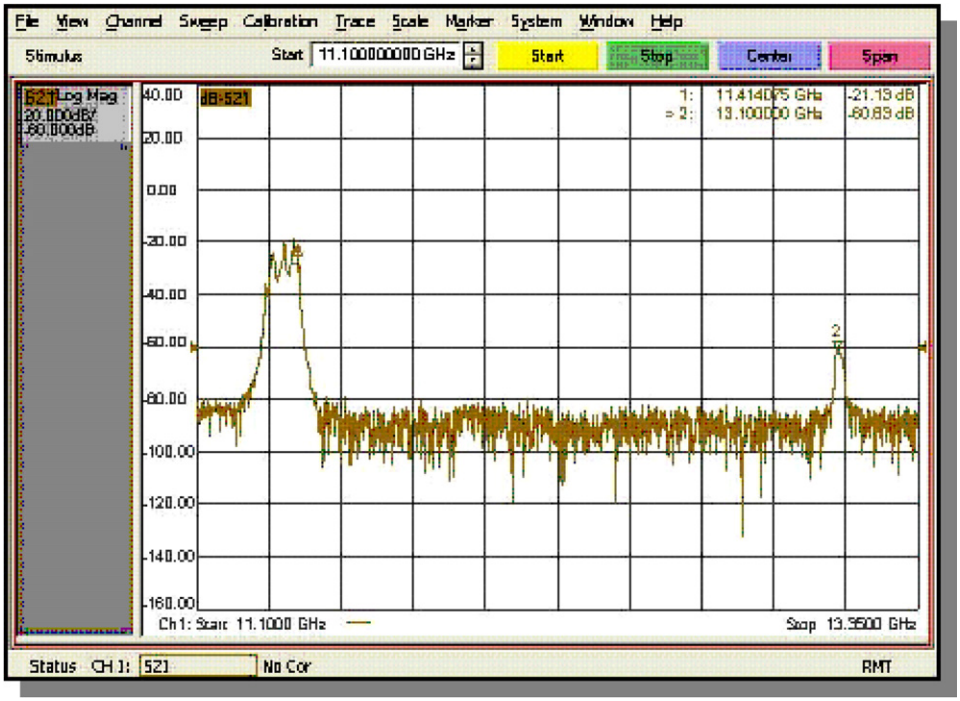

Fig. 15. Instrument screen-shot of the measurement of transmission coefficient for the opened stop band.

on the side cells are not; therefore the transmission coefficient coupler-antenna is greater than the transmission coefficient between the two antennas, as confirmed by the measurements.

The quality factor of the resonance has been measured and compared with the numerical ones. The Q factor of the $\pi/2$ mode in the case of stop-band close is reported in Table 5; the measured Q is lower than the calculated ones since the cavities are not brazed yet. In fact because of the number of cells (17), the electric continuity cannot be easily achieved with pressure given by the mechanical joints. With the bead pull technique we measured the electric field on axis [19] and therefore R/Q. To calculate the R/Q we have calibrated the bead form-factor comparing the perturbation induced by the perturbing object in a pill-box cavity working at 1.91 GHz on the TM_{010} mode with analytical results. Using different resonant modes of the pill-box cavity we have also checked that the form-factor does not depend on the frequency, within our measurement uncertainty.

The measured longitudinal electric field on axis, for the stop-band closed structure, is plotted in Fig. 17. Each field peak corresponds to a cell and the structure is "tuned" when the field amplitude is the same. The tuning procedure allows a field-flatness of the order of 3% at the nominal resonant frequency of 11.424 GHz. The mechanical precision achieved in the machining was such that the tuning did not require any automatic procedure, but only few small movement of the tuners. The measured R/Q per unit length is reported in Table 5 and it is in very good agreement with the simulation results. Comparison between simulation and measurements is possible only because the bead has been calibrated against known pill-0 box field.

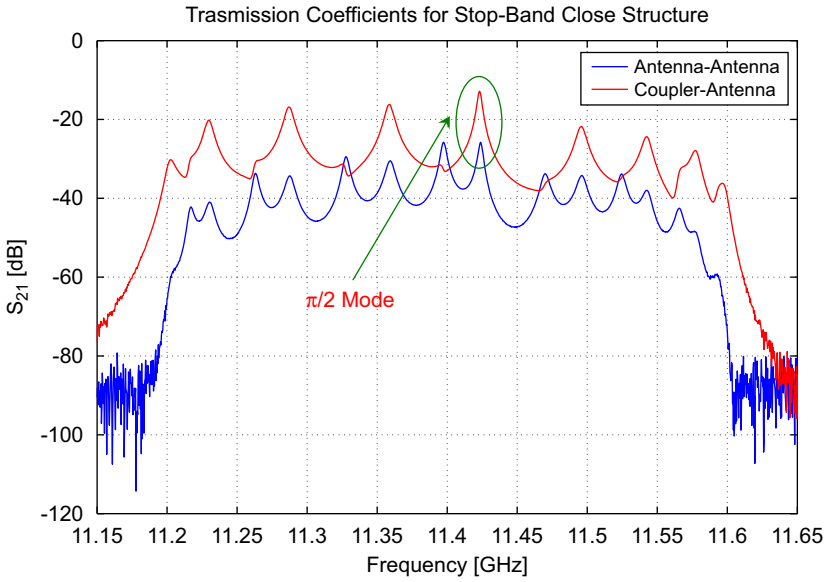

Fig. 16. Measurement of transmission coefficient between different point of the structure for the stop-band closed structure. The antennas are placed in the side cells while the coupler excite fields in the central cell.

Table 5
Quality and form factors measured on the stop-band close prototype compared with the numerical results

	HFSS	Superfish	Measurement
Q_0	7412	7101	5815
R/Q (Ω/m)	9452	9693	9150 ± 200

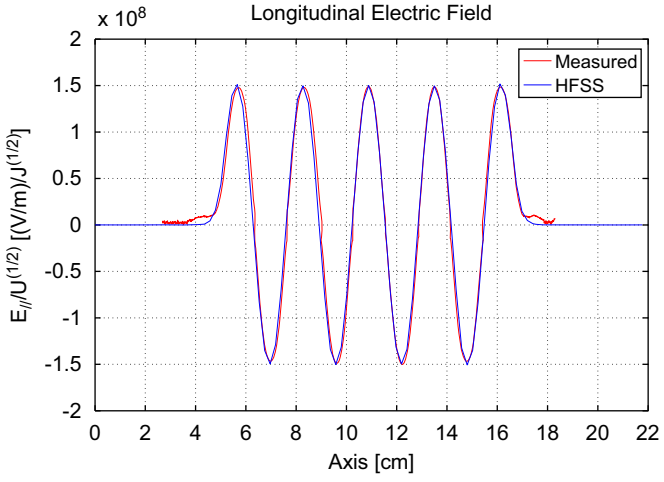

Fig. 17. Measured and simulated electric field on axis at the $\pi/2$-mode resonant frequency.

7. Conclusions

In the paper we presented the design of the bi-periodic X-Band accelerating structure for linearizing the longitudinal phase space in the Frascati Linac coherent light source (SPARC). The cavity, working on $\pi/2$ standing wave mode, has nine accelerating cells and eight axial coupling cells that have been tuned to close the stop-band between the two possible $\pi/2$ modes. The structure is fed by a coupler in the central cell and has been designed to obtain a 5 MV accelerating voltage. The analysis of the MP level has shown that the cavity can operate without problems up to 20 MV/m.

This paper demonstrates experimentally the feasibility of such a design in the X-Band. The main difficulties have been the choices of the coupling cell size, the large irises radius and the tight mechanical tolerances. The coupling cell sizes are chosen to minimize MP, while the relatively large iris radius (i.e. 4 mm against 1 cm cell radius) is needed for beam dynamics (i.e. geometrical aperture) requirements. It is well known that such a large iris radius makes the RF cavity very sensitive to imperfections and tight mechanical tolerances have been imposed in the mechanical fabrication of the copper prototype.

Quality factors, resonant frequency and dispersion curve measurements have been done on the copper prototype showing a good agreement with the expected values. Since the prototype was not brazed the reached quality factor was about 20% less than the theoretical one. Also the electric field measurement with the bead pull technique has demonstrated an excellent agreement with the theoretical calculations. In particular, to calculate the R/Q factor, the perturbing objects have been calibrated with a pill-box cavity. The final copper cavity is now ready to be brazed at LNF.

Acknowledgments

The authors are grateful to Alessandro Venzaghi and Daniele Giacopello for their help in the RF measurement.

V. Lollo deserves special thanks for the mechanical design and realization of the cavity prototypes.

References

[1] Technical Design Report for the SPARC Advanced Photo-Injector, Technical Report, LNF-INFN ROMA, 2003.
[2] P. Emma, X-Band RF harmonic compensation for the bunch compression in the LCLS, SLAC, LCLS-TN-01-1, 2001.
[3] D.T. Palmer. The next generation photoinjector, Ph.D. Thesis, Stanford University.
[4] M. Ferrario, et al., Homdyn Study for the LCLS RF Photoinjector, SLAC-PUB 8400.
[5] J.W. Wang, G.A. Loew, Measurements of Ultimate Accelerating Gradients in the SLAC Disk-Loaded Structure, 1985 PAC, Vancouver, BC, May 1985, SLAC-PUB 3597, March 1985.
[6] J.W. Wang, V. Nguyen-Tuong, G.A. Loew, RF break-down studies in a SLAC diskloaded structure, in: Proceedings of the 1986 Linear Accelerator Conference, Stanford, CA, June 1986, Slac-PUB-3490, April 1986.
[7] E. Tanabe, J.W. Wang, G.A. Loew, Voltage breakdown at X-band and C-band frequencies, in: Proceedings of the 1986 Linear Accelerator Conference, Stanford, CA, June 1986.
[8] J.W. Wang, G.A. Loew, Progress report on new RF breakdown studies in an S-band structure at SLAC, Presented at the 1987 PAC, Washington, DC, March 1987, SLAC-PUB-4247, February 1987.
[9] J.W. Wang, RF properties of periodic accelerating structures for linear colliders, SLAC Report-339, July 1989.
[10] K. Takata, in: Proceedings of the First Workshop on Japan Linear Collider (JLC), KEK, October 24–25, 1989.
[11] D.E. Nagle, E.A. Knapp, B.C. Knapp, Rev. Sci. Instrum. 38 (1967) 1583;
E.A. Knapp, B.C. Knapp, J.M. Potter, Rev. Sci. Instrum. 39 (1968) 979.
[12] P. Fernandes, R. Parodi, B. Spataro, F. Tazzioli, D. Tronc, Field computation and measurements on a biperiodic buncher structure, in: 1986 Linear Accelerator Conference, SLAC, Stanford University, Stanford, CA, June 2–6, 1986.
[13] B. Spataro et al., Studies on a Bi-Periodic X-Band Structure for SPARC, LNF-03/013(R), LNF-INFN, August 2003.
[14] P. Fernandes, R. Parodi, OSCAR2D, A computer code for the design of RF cavities and structures, in: Proceedings of the "LINAC 86 Conference," SLAC, June 1986, SLAC REPORT 303, p. 330.
[15] J.H. Billen, L.M. Young, Part. Acceler. 7 (4) (1976) 213.
[16] P. Fernandes, R. Parodi, Part. Acceler. 14 (1984).
[17] P. Fabbricatore, G. Gemme, R. Musenich, R. Parodi, S. Pittaluga, Experimental evidence of MP discharges in spherical cavities at 3 GHz, in: B. Bonin (Ed.), Proceedings of the Seventh workshop on RF superconductivity, Gif sur Yvette France, 1995, p. 385.
[18] P. Fernandes, R. Parodi, in: R. Lindstrom, L. Taylor (Eds.), Proceedings of Particles Accelerator Conference, IEEE catalog 89CH2387-9, Washington, DC, 16–19 March, 1987, p. 1857.
[19] D. Alesini, A. Falone, M. Migliorati, A. Mostacci, F. Palpini, L. Palumbo, B. Spataro, Nucl. Instr. and Meth. A 554 (2005) 1.
[20] ⟨http://www.ansoft.com⟩.